Generation of Warm Dense Matter using an Argon based Capillary Discharge Laser

A.K. Rossall*, G.J. Tallents

York Plasma Institute, University of York, Heslington, YO10 5DD, UK

Abstract

Argon based capillary discharge lasers operating in the extreme ultra violet (EUV) at 46.9 nm output up to 0.5 mJ energy per pulse at up to 10 Hz repetition rates are capable of focussed irradiances of 10^9 - 10^{12} W cm^{-2} and can be used to generate plasma in the warm dense matter regime by irradiating solid material. To model the interaction between such an EUV laser and solid material, the 2D radiative-hydrodynamic code POLLUX has been modified to include absorption via direct photo-ionisation, a super-configuration model to describe the ionisation dependant electronic configurations and a calculation of plasma refractive indices for ray tracing of the incident EUV laser radiation. A simulation study is presented, demonstrating how capillary discharge lasers of 1200 ps pulse duration can be used to generate warm dense matter at close to solid densities with temperatures of a few eV and energy densities up to 1×10^5 J cm^{-3}. Plasmas produced by EUV laser irradiation are shown to be useful for examining the properties of warm dense matter as, for example, plasma emission is not masked by hotter, less dense plasma emission as occurs with visible/infra-red laser target irradiation.

Keywords: EUV laser, High-energy-density matter, Atomic Physics, Hydrodynamic modelling, Strongly coupled plasma
2010 MSC: 00-01, 99-00

1. Introduction

Considerable advances have been made in higher fluence EUV and x-ray laser technology as demonstrated by free-electron lasers [1, 2] and capillary discharge lasers [3, 4]. With higher fluences now available, EUV and x-ray lasers can be used to directly generate strongly coupled plasma. These plasmas are produced by irradiating solid targets with EUV/x-ray lasers, heating the sample via direct photo-ionization, resulting in typically lower temperatures

*Corresponding author
Email address: andrew.rossall@york.ac.uk (A.K. Rossall)

and higher densities than the traditional laser produced plasma, generated using infra-red, optical and UV pulses. By reducing the wavelength into the EUV/x-ray region, the photon energy, E_p, becomes sufficient to directly photo-ionise elemental components, transferring a set amount of energy ($E_p - E_i$) to the ejected electron. Reducing the lasing wavelength to the EUV/soft x-ray region allows for a tighter focus (due to a reduction in the diffraction limit) and enables the laser to penetrate into the solid material, as the critical density at these wavelengths are typically higher than solid. Due to the unique properties of plasmas generated by EUV/x-ray lasers, these plasmas can contribute to our understanding of warm dense matter. The ability to couple a correct equation-of-state with an accurate model of radiation transport is essential in order to achieve inertial confinement fusion as the pre-ignition fuel is in the warm dense matter regime.

To promote research and to accelerate the development of industrial applications, there has been significant motivation to produce compact and affordable EUV/x-ray sources for use in parallel with large scale facilities such as the free-electron laser FLASH [5] based at DESY. The research group at Colorado State University (CSU) have developed a table-top size soft x-ray laser system [6, 7, 8] based upon capillary discharge excitation of an Ar gas producing a large soft x-ray amplification.

The work presented here utilises a novel combination of 2D fluid code modelling (POLLUX) with a rapid atomic physics algorithm to simulate the EUV/x-ray interaction with solid material, the expected energy deposition within the target, the produced plasma parameters and the subsequent ablative flow away from the target. A simulation study it is presented to demonstrate the capability of EUV capillary discharge lasers for the generation of warm dense matter.

2. POLLUX

2.1. Hydrodynamic code

The 2D Eulerian hydrodynamic code POLLUX [9, 10], written at the University of York, was originally developed to model moderate irradiance ($\geq 10^{10}$ W cm^{-2}) laser irradiation of a solid target producing a strongly ionized plasma which further interacts with the incident laser beam. The code solves the three first-order quasi-linear partial differential equations of hydrodynamic flow using the flux corrected transport model of Boris and Book [11] with an upwind algorithm [12] for the first term. Energy is absorbed by the plasma electrons through inverse bremsstrahlung and direct photo-ionization and is distributed through electron-ion collisions. The energy transfer rate between the electrons and ions is calculated using the smaller value of the Spitzer plasma collision frequency [13] or the electron-phonon collision frequency [14]. For calculation of the equation-of-state (EOS) variables, POLLUX utilizes in-line hydrodynamic EOS subroutines from the Chart-D [15] equation-of-state package developed st Sandia National Laboratories. As POLLUX uses an explicit solver, a maximum Courant number of $C \sim 1$ is required. When accounting for both spatial directions the Courant number is given by,

$$C = \frac{u_x \Delta t}{\Delta x} + \frac{u_y \Delta t}{\Delta y} \sim 1. \quad (1)$$

Here u_x and u_y are magnitudes of the particle velocities in the respective directions, Δt is the time step and Δx,Δy are the cell spatial dimensions. The Courant-Friedrichs-Lewy condition [16] is not the only constraint on simulation parameters, however, it is the most restrictive.

2.2. Atomic physics algorithm

The atomic physics algorithm utilises a superconfiguration approach to calculate atomic scattering factors in the EUV and X-ray for partially ionised plasmas. Detailed level structure is initially obtained by using the Flexible Atomic Code (FAC) [17] to solve the radial wave equation. This structure is post-processed to group energetically similar levels into 'supershells', where the average energy, $\langle E \rangle_{SS}$ is weighted by the degeneracy (g_m) and given by

$$\langle E \rangle_{SS} = \frac{\sum_m g_m E_m}{\sum_m g_m}, \quad (2)$$

where E_m is the energy of a single detailed level.

Ionisation and excited level populations are determined assuming local thermodynamic equilibrium, an assumption which is justified on hydrodynamic timescales of $>$ ps, as the highly non-equilibrated plasma initially created equilibrates on the order of 10s of fs [18]. Photoionisation cross-sections for each ionisation stage and superconfiguration level are calculated assuming a E^{-3} photon energy dependance, and a configuration specific constant ($A\,(n, Z)$) determined using data from FAC. This approximation allows for an analytical solution to the Kramers-Kronig relation where the atomic scattering factor $f_1^0(E)$ is given by

$$f_1^0(E) = Z^\star + \frac{1}{\pi r_e hc}\left(\sum_Z \sum_n \frac{A(n,Z)}{2E^2} \log\left(|1 - \frac{E^2}{E_{i,n}^2}|\right)\right), \quad (3)$$

where $Z^\star$ is the number of bound electrons, Z is the ionisation stage, n is the supershell number, E is the photon energy and $E_{i,n}$ is the binding energy of an electron in supershell n of an ion with charge Z. The time averaged effects of the ionisation potential depression is accounted for in the binding energy, $E_{i,n}$, using the Stewart-Pyatt model [19, 20]. This model has shown reasonable agreement with data from the CXRO for cold, solid carbon, as is shown in figure 1, however, it is worth noting that the E^{-3} approximation breaks down for materials with $Z \geq 13$, especially in the energy region of $E < 100eV$.

The atomic physics algorithm is used to calculate the populations, free electron density and refractive index for each cell within the fluid code POLLUX and is updated for each time step. The populations and free electron density are used in the calculation of the laser absorption as outlined previously [21] and the refractive index is calculated to simulate the effect of the expanding

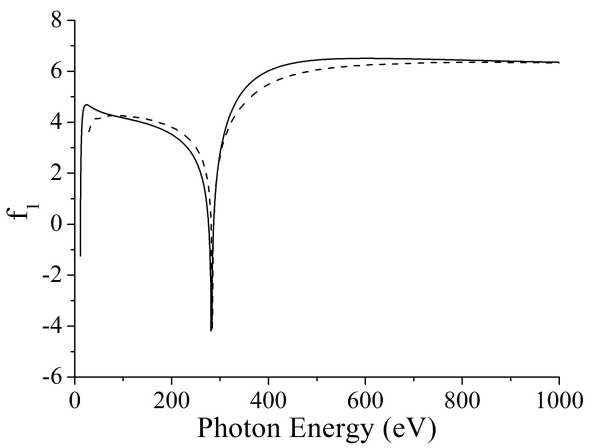

Figure 1: Scattering factor, f_1, for cold, solid carbon as a function of photon energy. A comparison is made between our algorithm (solid line) and data from the Centre for X-ray Optics (CXRO) at Lawrence Berkeley National Laboratory (dashed line).

plasma on the path of the laser pulse. As the free electron approximation for the refractive index is not valid in the EUV, the value of $f_1^0(E)$ from equation 3 is used to calculate the real component of the refractive index. The refractive index is input into the ray tracing routine of POLLUX for each time step.

3. Results and discussion

Figure 2 indicates the geometry of the simulation environment, with the laser incident from right to left irradiating a planar target with surface at x=0. Figures 2(a) and 2(b) show the ablation profiles for a capillary discharge laser, with photon energy 26eV, irradiance of 5×10^9 W cm^{-2} and focal spot diameter (FWHM) of 500nm after (a) 1 pulse and (b) 4 pulses. A depth of 4.2μm is ablated after 4 pulses with a lateral hole size of 1.3μm (FWHM). Figures 2(c) and 2(d) show how the ablation profile changes as the focal spot diameter is reduced, approaching the diffraction limit. For a focal spot diameter of 200nm, figures 2(c) and 2(d) show the ablation profiles after (c) a single pulse and (d) two pulses for an irradiance of 5×10^9 W cm^{-2}. After the second pulse, an ablated depth of 2.4μm is observed with a lateral hole size of 644nm (FWHM). This indicates the potential of this technology for meso-scale (100nm - 1μm) machining and the capability of the computational algorithms to optimise the ablative characteristics for specific applications. By comparing simulation results with ablation profiles obtained experimentally via atomic force microscopy, the code has been benchmarked using realistic focussing conditions and these results are published [21, 22].

It is observed that plasma refractive index effects become significant at irradiances greater than 1×10^{10} W cm^{-2}, resulting in the beam both self-focussing

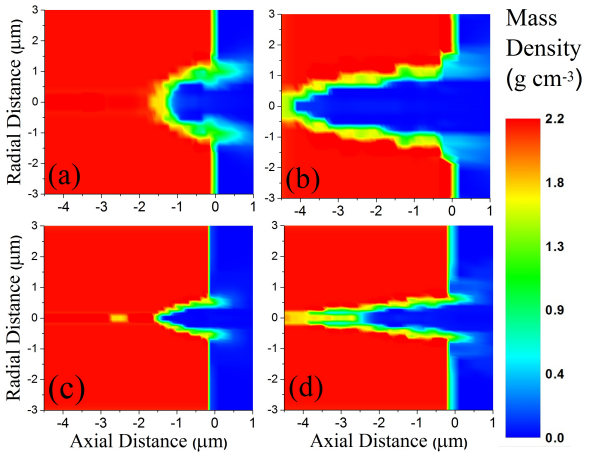

Figure 2: (Color online) Ablation profiles at $t = 1300$ps for an irradiance of 5×10^9 W cm^{-2} for focal spot diameters (FWHM) of 500nm after (a) 1 pulse and (b) 4 pulses, and 200nm after (c) 1 pulse and (d) 2 pulses.

and diverging in different regions of the produced plasma. For this reason an efficient, temperature dependant model for the atomic scattering factors is required to adequately simulate the EUV laser-solid interaction. For the simulation results shown here, the simple analytical model described above was used, however for higher Z materials a more detailed description will be required. This will most likely be in the form of an interpolation routine using opacity tables generated from existing codes. In addition to the refractive index effects, 'bleaching' of the target is observed in the values of the bound-free opacity, as shown in figure 3, and is analogous to that observed in FEL interactions only on a picosecond timescale.

An electron temperature and particle density plot is shown in figure 4 for a plasma produced by an EUV laser of irradiance 1×10^{10} W cm^{-2} at the time of peak temperature, t=200ps. The dashed line indicates the region of highest energy density, with an electron temperature of 2 -3 eV and a particle density of 10^{23} cm^{-3}. This is shown in more detail in figure 5 which shows the energy density profiles, along the laser axis, after 200ps, 300ps and 400ps of irradiation. The regions of highest energy density are in the close to solid region of the plasma and not in the expanding plasma plume as is usually the case for plasmas produced by optical and infra-red lasers. As a result, emission from the strongly-coupled plasma is less likely to be masked by the hotter and less dense plasma plume. Simulations indicate that increasing the irradiance to 1×10^{12} W cm^{-2} will produce plasma with energy densities exceeding 1×10^5 J cm^{-3}.

One consideration with studies of equation-of-state (EOS) parameters or plasma opacity is the uniformity of the sample heating. Perfect volumetric heating would be ideal, however temperature and density gradients arise due to

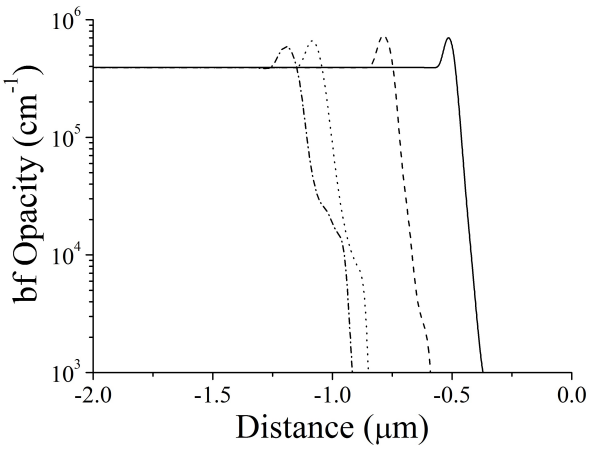

Figure 3: Bound-free opacity values at t=200ps (solid), t=400ps (dashed), t=600ps (dotted) and t=800ps (dash-dot) during the EUV laser solid interaction. For each time, a rapid drop in bound-free opacity indicates the propagation of the laser.

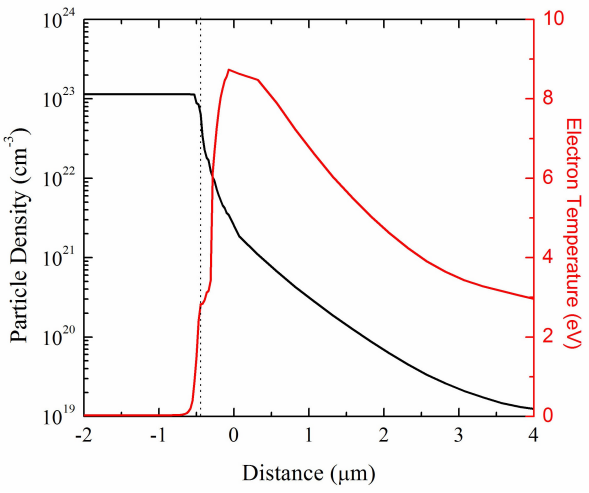

Figure 4: (Colour online) Temperature and density plot, along the laser axis, at the time of peak temperature, t=200ps, for an EUV pulse of irradiance 1×10^{10} W cm^{-2}. The dotted vertical line indicates a region of interest with a temperature of 2 - 3eV at a particle density of 10^{23} cm^{-3}.

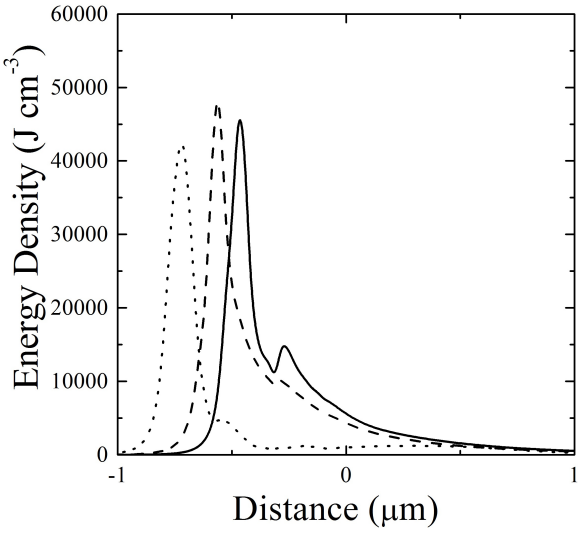

Figure 5: Energy density plot along the laser axis for an EUV pulse of irradiance 1×10^{10} W cm^{-2} at t=200ps (solid line), 300ps (dashed line) and 400ps (dotted line).

non-uniformities associated with heat flow through the target. This is especially prevalent in laser-solid interactions as the heating usually occurs from one side of the sample, as is the case in this study. However, the change in dominant absorption mechanism to photo-ionisation results in the majority of the laser energy being absorbed within the solid material. Due to the short absorption length of 26eV photons in parylene-N, 99% of the beam irradiance is absorbed within a 100nm depth, resulting in the energy density peaks seen in figure 5. The plasma emission from the high energy density region is not masked by hotter, less dense plasma emission as would normally occur with visible/infrared laser target irradiation. A sufficiently fast camera or streak camera would be able to temporally resolve the dominant emission from these regions. A linear approximation for the temperature and density gradients, as done previously [23], would be suitable for EOS and opacity modelling. The particle density drops less than an order of magnitude and the temperature changes by $\sim$ 2eV, both with an approximately linear relationship over the high-energy density region.

4. Conclusion

Argon based capillary discharge lasers operating in the extreme ultra violet (EUV) at 46.9 nm can be used to generate plasma in the warm dense matter regime by irradiating solid material. The 2D radiative-hydrodynamic code POLLUX has been modified to include absorption via direct photo-ionisation, a super-configuration model to describe the ionisation dependant electronic con-

figurations and a calculation of plasma refractive indices for ray tracing of the incident EUV laser radiation. This simulation study has demonstrated how capillary discharge lasers can be used to generate warm dense matter at close to solid densities with temperatures of a few eV and energy densities up to 1×10^5 J cm^{-3}.

Plasmas produced by EUV laser irradiation are shown to be useful for examining the properties of warm dense matter as plasma emission from the strongly coupled plasma is not masked by hotter, less dense plasma emission as occurs with visible/infra-red laser target irradiation.

5. Acknowledgements

This work has been funded by EPSRC grant EP/J019402/1.

References

[1] J. T. Costello. J. Phys.: Conf. Ser. **88** 012057 (2007).

[2] N. Berrah, J. Bozek, J. Costello, et al. J. Mod. Opt. **57** 1015 (2010).

[3] B. Benware, C. Macchietto, C. Moreno, et al. Phys. Rev. Lett. **81** 5804 (1998).

[4] G. Vaschenko, A. G. Etxarri, C. S. Menoni, et al. Opt. Lett. **31** 3615 (2006).

[5] V. Ayvazyan, N. Baboi, J. Bähr, et al. Eur. Phys. J. D **37** 297 (2005).

[6] B. R. Benware, C. H. Moreno, D. J. Burd, et al. Opt. Lett. **22** 796 (1997).

[7] J. J. Rocca, V. Shlyaptsev, F. Tomasel, et al. Phys. Rev. Lett. **73** 2192 (1994).

[8] J. J. Rocca, F. G. Tomasel, M. C. Marconi, et al. Phys. Plasmas **2** 2547 (1995).

[9] G. J. Pert. J. Plasma Phys. **41** 263 (1989).

[10] G. J. Pert. J. Comput. Phys. **49** 1 (1983).

[11] J. Boris, D. Book. J. Comput. Phys. **20** 397 (1976).

[12] R. Courant, E. Isaacson, M. Rees. Commun. Pure Appl. Math. **5** 243 (1952).

[13] L. Spitzer, R. Härm. Phys. Rev. **89** 977 (1953).

[14] J. B. Lee, K. Kang, S. H. Lee. Mater. Trans. **52** 547 (2011).

[15] S. L. Thompson. Sandia National Laboratories Report **SC-RR-70-2** (1970).

[16] R. Courant, K. Friedrichs, H. Lewy. IBM J. Res. Dev. **11** 215 (1967).

[17] M. F. Gu. Can. J. Phys. **86** 675 (2008).

[18] V. Aslanyan, G. J. Tallents. Phys. Plasmas **21** 062702 (2014).

[19] J. C. Stewart, K. D. Pyatt. Astrophys. J. **144** 1203 (1966).

[20] T. R. Preston, S. M. Vinko, O. Ciricosta, et al. High Energ. Dens. Phys. **9** 258 (2013).

[21] A. K. Rossall, V. Aslanyan, G. J. Tallents. Proc. SPIE **8849** 884912 (2013).

[22] A. K. Rossall, I. Kuznetsovi, V. Aslanyan, et al. In preparation for Appl. Phys. Lett. (2015).

[23] T. Nagayama, J. E. Bailey, G. A. Rochau, et al. Rev. Sci. Instrum. **83** 10E128 (2012).